Exsolution of Co-Fe Alloy Nanoparticles on the $PrBaFeCoO_{5+\delta}$ Layered Perovskite Monitored by Neutron Powder Diffraction and Catalytic Effect on Dry Reforming of Methane

Praveen B. Managutti[a,f], Haoran Yu[b], Olivier Hernandez[a,e], Carmelo Prestipino[a], Vincent Dorcet[a,d], Haiqian Wang[b], Thomas Hansen[c], and Mona Bahout*[a]

[a] Univ. Rennes, CNRS, ISCR (Institut des Sciences Chimiques de Rennes) – UMR 6226, F-35000 Rennes, France
[b] Hefei National Laboratory for Physical Science at the Microscale, University of Science and Technology of China, Hefei, Anhui 230026, People's Republic of China
[c] Laue-Langevin Institute, 71 avenue des Martyrs CS 20156, 38042 Grenoble Cedex 9,France
[d] Univ Rennes, CNRS, ScanMAT – UAR 2025, F-35000 Rennes, France
[e]Nantes Université, CNRS, Institut des Matériaux de Nantes Jean Rouxel, IMN, F-44000 Nantes, France
[f]Chemical Crystallography Laboratory, Khalifa University of Science and Technology, Abu Dhabi, P.O. BOX 127788, United Arab Emirates

Abstract

Reversible exsolution and dissolution of metal nanoparticles in complex oxides has been investigated as an efficient strategy to improve the performance and durability of the catalysts for thermal and electrochemical energy conversion. Here *in situ* exsolution of Co-Fe alloy nanoparticles from the layered perovskite $PrBaFeCoO_{5+\delta}$ (PBFC) and their dissolution back into the oxide host have been monitored for the first time by *in situ* neutron powder diffraction and confirmed by X-ray diffraction and electron microscopy. Catalytic tests for dry reforming of methane showed stable operation over ~100 h at 800 °C with negligible carbon deposition (< 0.3 $mg/g_{cat}\cdot h$). The CO_2 and CH_4 conversions are among the highest achieved by layered double perovskites. The cyclability of the PBFC catalyst and the potential to improve the catalytic activity by adjusting composition, size, and the nanoparticles distribution would pave the way for highly efficient energy conversion applications.

Keywords: Layered double perovskite, Co-Fe alloy nanoparticles, bimetallic exsolution, *in situ* neutron diffraction, dry reforming of methane.

1. INTRODUCTION

Metal nanoparticles dispersed on oxide surfaces have been largely investigated as catalysts in several energy conversion thermochemical and electrochemical processes including solid oxide cells and dry reforming of methane (DRM). Generally, the particles prepared by conventional wet impregnation or infiltration routes are usually subject to long-term stability issues due to sintering or coking resulting in irreversible catalyst deactivation.[1-6] The exsolution approach has attracted much interest to produce supported metal nanocatalysts with higher thermal stability to address the sintering issue, and enhanced coking resistance in comparison with supported metal catalysts produced by conventional methods.[7] The general principle of exsolution involves the substitution of active elements into an oxide lattice during the synthesis in air, which will exsolve (precipitate) on the surface in the form of catalytically active nanoparticles (NPs) under reducing conditions.[8] In some cases, the exsolved particles may dissolve back into the oxide lattice under oxidative conditions and be self-regenerated by redox cycling which relieves coarsening and agglomeration issues and enhances catalyst lifetime.[9-10] This solution, referred to as "intelligent catalyst", has been applied to automotive emissions-control to address the sintering issue.[11]

Here, the layered double perovskite, $PrBaFeCoO_{5+\delta}$ (PBFC), was selected because iron-based double perovskites have excellent resistance against coking and sulfur poisoning[12] while cobalt promotes the exsolution of Co–Fe alloy nanoparticles for the catalytic activity. Indeed, the Fe-only composition, $PrBaFe_2O_{5+\delta}$, does not exsolve Fe metal under reducing conditions.[13] The synergistic effects of Fe and Co would improve catalytic activity and stability by forming supported metal alloys. Another advantage of PBFC relates to the redox reversibility of metal

NPs exsolution/dissolution by switching between reducing and oxidizing atmospheres, as reported for $Pr_{0.8}Sr_{1.2}(Co,Fe)_{0.8}Nb_{0.2}O_{4+\delta}$[14] and $La_{0.3}Sr_{0.73}Cr_{0.3}Fe_{0.6}Co_{0.1}O_{3-\delta}$.[15]

In this work we monitored the exsolution of Co-Fe NPs from PBFC using *in situ* neutron diffraction under wet 5% H_2/He (3% H_2O) and their dissolution into the layered perovskite under flowing air. Besides examining the crystal structure throughout a redox cycle, we checked the catalytic activity of the PBFC material for DRM[8, 16] illustrated by the following reaction:

$$CH_4 + CO_2 \leftrightarrow 2\ CO + 2\ H_2 \quad \Delta H° = 247\ kJ\ mol^{-1} \qquad \text{(Eq. 1)}$$

One of the most limiting factors in dry reforming is coke deposition on the catalyst through the Boudouard equilibrium ($2\ CO \leftrightarrow C_{ads} + CO_2$, $\Delta H° = -172\ kJ\ mol^{-1}$)[17-19] and methane cracking ($CH_4 \leftrightarrow C_{ads} + 2\ H_2$, $\Delta H° = 75\ kJ\ mol^{-1}$)[20] resulting in rapid catalyst deactivation.[8] Self-regeneration of the catalyst by redox cycling can mitigate coking and particle agglomeration issues for long-term operation making the DRM process more industrially viable.[21]

EXPERIMENTAL SECTION

Materials Synthesis and Characterization

Polycrystalline PBFC was prepared by the Pechini method. Stoichiometric amounts of $Pr(NO_3)_2 \cdot 6H_2O$ (Aldrich, 99.9%), $Ba(NO_3)_2$ (Aldrich, 99%), $Fe(NO_3)_2 \cdot 9H_2O$ (Aldrich, 98%), $Co(NO_3)_2 \cdot 6H_2O$ (Aldrich, 98.5 %) were dissolved in distilled water with ethylene glycol (EG), citric acid (CA) in the molar ratio to the total metal ions (M) CA:EG:M of 1:3:1.5. Ammonia was added to fix the pH at 8 to enhance cation binding to the citrate and avoid the precipitation of individual hydroxides.[22] The solution was continuously stirred on the hot plate at 80 °C for 2 h to evaporate water. The resulting viscous liquid was heated to 250 °C, causing self-ignition and formation of a resin, which was calcined at 550 °C. After annealing in air at 1100 °C for 6 h, a layered double perovskite, referred as S-PBFC, was formed, as evidenced by XRD (Figure 1a, black curve). The phase evolution was analyzed after annealing the S-PBFC powder at 850

°C (8 h) under 5% H_2/N_2 (3% H_2O) resulting in the reduced composition, R-PBFC. Redox reversibility was examined by annealing the R-PBFC powder at 800 °C in air overnight resulting in the oxidized sample, O-PBFC which was further reduced under hydrogen. The X-ray diffraction (XRD) patterns were collected using a Bruker AXS D8 Advance diffractometer in Bragg-Brentano geometry equipped with a Ge a (111) Johansson focusing primary monochromator (Cu-$K_{\alpha 1}$) and a silicon strip Lynxeye detector. Data were analyzed by the Rietveld method with the FullProf program[23] and its graphic interface WinPLOTR[24]. The oxygen content (5+δ) was determined *via* iodometric titration against standardized sodium thiosulfate.[25] The morphology of the samples was observed with field emission scanning electron microscopy (JEOL JSM-7100F). All the samples were examined using 5−10 kV imaging to reduce charging. Microstructure and element distribution were probed by Scanning Transmission Electron Microscopy (STEM) using a JEOL 2100 LaB_6 instrument operating at 200 kV equipped with Energy Dispersive X-ray Spectroscopy (EDS) (OXFORD X-MAX^N 80T). The powder samples were crushed in dry ethanol and a droplet of the suspension was mounted on a carbon-coated copper grid.

In situ neutron diffraction

The neutron diffraction patterns have been collected in the temperature range of 20-900 °C on the high-flux two-axis D20 neutron diffractometer at the high-flux reactor of the *Institut Laue-Langevin* (ILL, Grenoble, France).[26] The set-up has been described previously.[25] A take-off angle of 90 ° from the (115) plane of a germanium monochromator was chosen, giving a wavelength λ ~ 1.54 Å and an optimum resolution, $\Delta d/d \sim 3\times10^{-3}$, while retaining a high flux on the sample (~ 1.6×10^7 n cm^2 s^{-1}). A sample of ~ 2.0 g was loaded at the center of a quartz tube (8 mm inner diameter). Two K-type thermocouples were placed in the quartz tube; one a

few mm above the sample to monitor the temperature and another below the sample to adjust the temperature. The temperature profile used in the neutron experiment is displayed in Fig. 1.

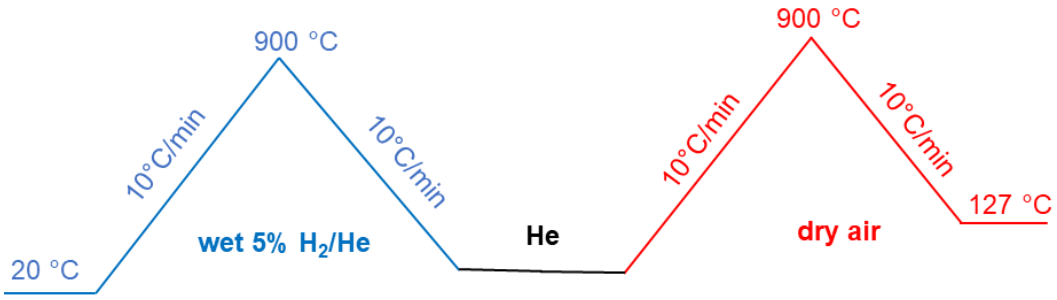

Figure 1. Temperature profiles used in the neutron experiment.

Data were collected during heating and cooling. A single data set covers a temperature change of 10 °C. The background was modeled using linear interpolation between ~ 60 points and two asymmetry parameters were refined below $2\theta = 55°$. The unit cell parameters and zero-point shift were refined. The peak profile was modeled using a Thompson-Cox-Hastings pseudo-Voigt profile function. The atomic coordinates, the oxygen occupancy, and the isotropic displacement parameters (B_{iso}) of all the atoms were refined.

Evaluation of catalytic activity for dry reforming of methane (DRM)

The catalytic activity for the DRM reaction (Eq. 1) was evaluated in a fixed bed quartz reactor (i. d. = 6 mm). It can be inferred from the results of *in situ* neutron diffraction that the exsolution of Co-Fe NPs occurred at a temperature of 850 °C, or higher with a higher rate. Therefore, polycrystalline S-PBFC (200 mg) and quartz powder (800 mg 40-60 mesh) were loaded in the reactor and heated in pure H_2 at 900 °C for 1 h to activate the catalyst and ensure the exsolution of the Co—Fe NPs from the oxide host in a short time. We also adopt those conditions for better comparison with the literature.[27-29] After purging the reactor with argon for 1 h to remove residual H_2, the reactant gases (20 % CH_4, 20 % CO_2, balanced with argon) were introduced at a total flow rate of 100 $mLmin^{-1}$. The gaseous hourly space velocity (GHSV) of 3.0×10^4 $mLgcat^{-1}h^{-1}$ was maintained throughout the test. The reaction products were analyzed online by

gas chromatography (GC9790, FULI), and the flow rate of the tail gas was measured by a soap film flowmeter. The DRM tests were performed on cooling from 900 to 800 °C with a temperature step of 50 °C. CO_2 conversion and CO selectivity were calculated using the following equations: [30-31]

$$Conv_{CO_2} = \frac{[CO_2]_{in} - [CO_2]_{out}}{[CO_2]_{in}} \times 100\ \%,$$

$$Selectivity_{CO} = \frac{[CO]_{out}}{[CO]_{out} + [CO_2]_{out}} \times 100\ \%$$

where $[CO_2]_{in}$, $[CO_2]_{out}$ and $[CO]_{out}$ are the molar flow rates at the inlet and outlet of the reactor. The coking rate (amount of carbon deposited per gram of catalyst and per hour) was evaluated by temperature programmed oxidation (TPO) using thermogravimetric (TG) analysis (STA 449 F3, NETZSCH, Germany). Around 30 mg of powder containing 80 wt.% of the quartz sand and 20 wt.% of the spent catalyst (unable to be removed from quartz sand) was placed in an alumina crucible and heated under N_2 (10 sccm) to 800 °C at 10 °C min^{-1} to remove the adsorbed gas molecules. After cooling to room temperature, the sample was heated to 1000 °C in dry air (60 sccm) at 10 °C min^{1}. The mass loss detected in the high-temperature stage above 600 °C relates to the amount of carbon deposition.

2. RESULTS AND DISCUSSION

Structure characterization

To achieve phase purity, the PBFC powder was annealed at 1100 °C in air for 6 h. The XRD pattern displayed in Fig. 2a shows two distinct doublets in the $2\theta \sim 45°–50°$ and 65°–70° ranges, typical of the tetragonal layered double perovskites of space group, S.G. *P*4/*mmm* (JCPDS#00-061-0290) in agreement with previous results reported for $PrBaCoFeO_{5+\delta}$.[32]

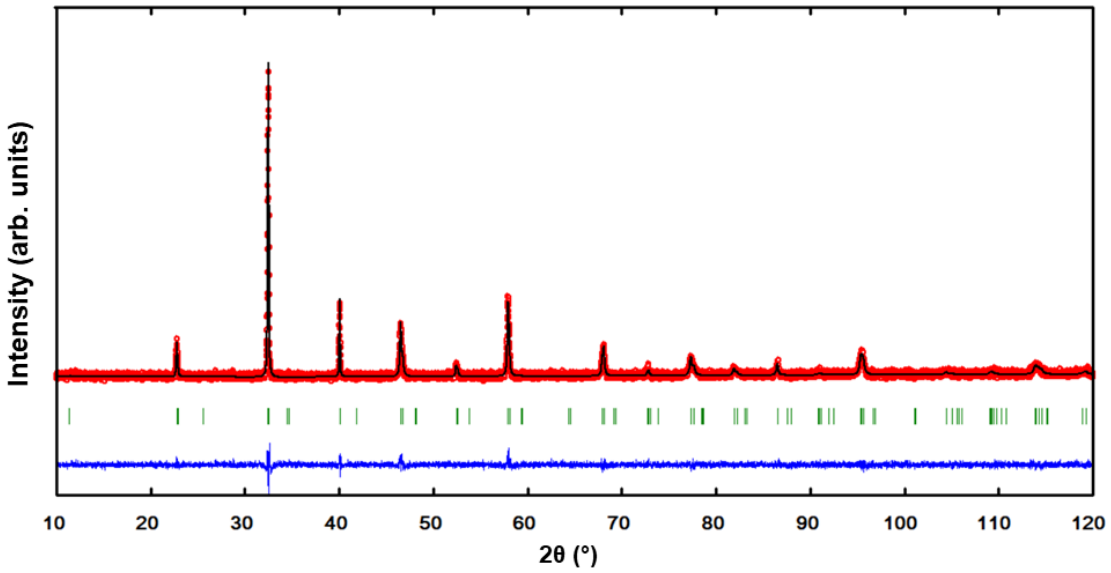

Figure 2a. Rietveld plot of X-ray diffraction data for S-PBFC at 20 °C.

The redox stability and phase reversibility were evaluated by annealing the powder samples alternatively under wet 5% H_2/Ar and ambient air for 8 h. Figs 2b and 2c displaying the XRD patterns of PBFC after the redox tests demonstrate the excellent stability as suggested by the retention of the tetragonal structure. After the reducing treatment under hydrogen, the XRD pattern (Fig. 2b) exhibits extra peaks at 2θ ~ 44, 51 and ~ 65.4° assigned to the exsolution of Co-Fe alloy (S.G. *Im*-3*m*, JCPDS #01-071-7173) nanoparticles, as reported for $NdBaFe_{2-x}Co_xO_{5+\delta}$ and $Sr_2Fe_{1.35}Mo_{0.45}Co_{0.2}O_6$.[33] The intensity of the other peaks from Co-Fe alloy falls below the diffraction detection limit due to the very small amount and nano size of the exsolved particles. It is useful to mention that the only Fe composition, $PrBaFe_2O_{5+\delta}$, did not exsolve metal NPs under similar reducing conditions.[13] There are also small peaks in the XRD pattern, at 2θ ~ 26.7, 29.7 and 30.6° assigned to the $Ba_6Pr_2Fe_4O_{15}$ impurity phase (S.G. $P6_3mc$, JCPDS#00-061-0536), as reported for the reduction of $PrBaFe_{1.8}Co_{0.2}O_{5-\delta}$.[34] Because the reflections from Co-Fe and $Ba_6Pr_2Fe_4O_{15}$ are close to XRD detection limits, those phases could be only roughly estimated at ~ 6 wt. % and ~ 4 wt. %, respectively (Table 1).

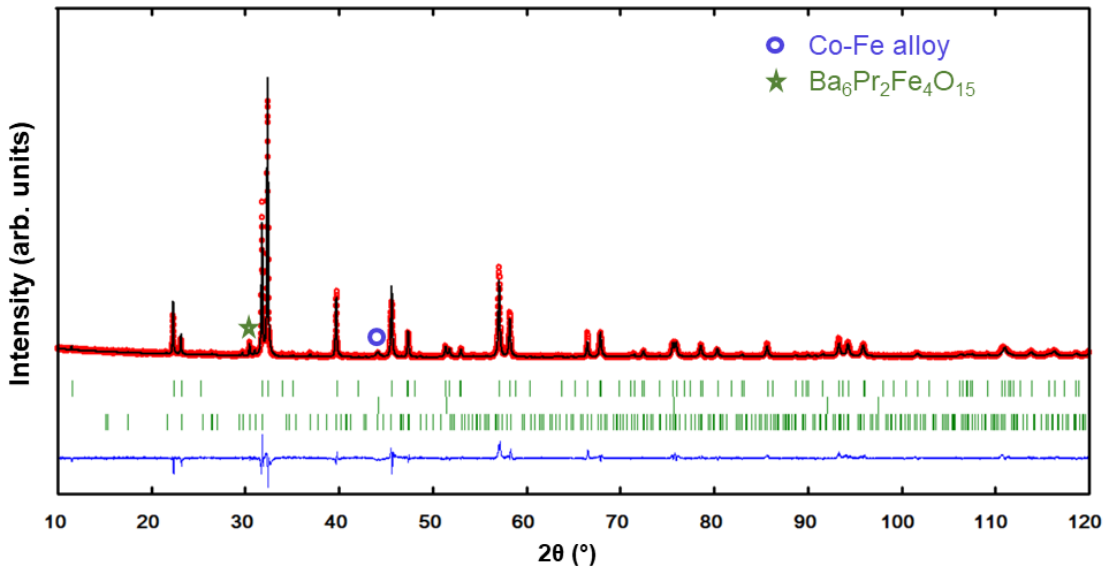

Figure 2b. Rietveld plot of X-ray data for R-PBFC. First, second and third row tick marks refer to R-PBFC, Co-Fe alloy, and $Ba_6Pr_2Fe_4O_{15}$, respectively.

After annealing the R-PBFC sample in air at 800 °C, the XRD pattern of O-PBFC (Fig. 2c), shows the reflections of the only layered phase with lattice parameters close to those of the original composition (Table 1) due to small variations in oxygen-content. In contrast to the oxidation of $Sr_2Fe_{1.5}Mo_{0.45}Co_{0.2}O_{6-\delta}$,[33] we were not able to detect the presence of $CoFeO_x/CoFe_2O_4$ in the XRD pattern of O-PBFC, which suggests faster dissolution of Co-Fe into the bulk and excellent redox cyclability of PBFC, as reported for $Pr_{0.4}Sr_{0.6}Co_{0.2}Fe_{0.7}Nb_{0.1}O_{3-\delta}$.[35]

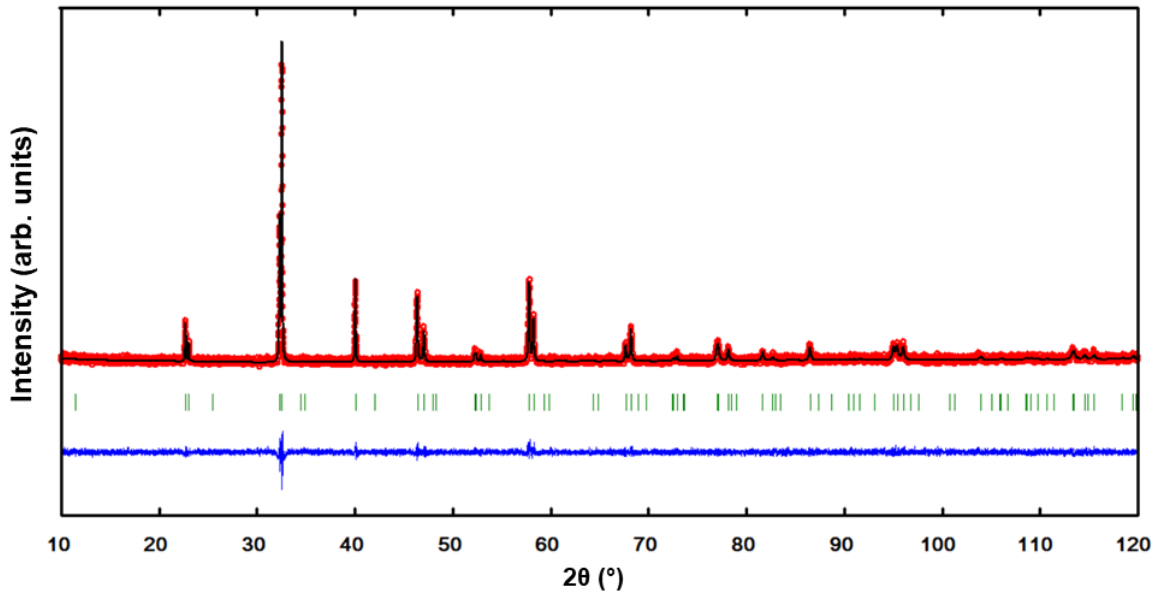

Figure 2c. Rietveld plot of X-ray data for O-PBFC.

Table 1. Lattice parameters of $PrBaFeCoO_{5+\delta}$ (S.G. *P4/mmm*) after various treatments.

Phase	*a* (Å)	*c* (Å)	*V* (Å^3)	Reliability factors (Rietveld)
S-PBFC	3.91626 (2)	7.7575 (1)	118.977 (2)	R_{wp} (%) = 9.36, R_p (%) = 6.85, χ^2 = 2.1
***R-PBFC**	3.97320 (4)	7.66475 (8)	120.998 (2)	R_{wp} (%) = 9.7, R_p (%) = 6.97, χ^2 = 2.9
O-PBFC	3.91757 (4)	7.71880 (9)	118.463 (6)	R_{wp} (%) = 9.53, R_p (%) = 7.27, χ^2 = 2.7

*Phase fractions: R-PBFC (~ 91 wt. %), Co-Fe (~ 6 wt. %), and $Ba_6Pr_2Fe_4O_{15}$ (~ 4 wt. %).

Microstructure analysis

Fig. 3 shows the surface morphology after reduction, reoxidation and re-reduction. The SEM image after reduction shows spherical nanoparticles on the surface (Fig. 3a) with size distribution expanding from 25 to 100 nm (Fig. 3b). After reoxidation, the smooth surface of O-PBFC suggests that the exsolved NPs have dissolved into the perovskite lattice (Fig 3c). The small pyramidal particles remaining on the surface were identified as $BaCO_3$ (Fig. S1). The formation of barium carbonate is due to the surface segregation of Ba^{2+} ions which react with CO_2 to form $BaCO_3$ as observed for $GdBaCo_2O_{5+\delta}$ and $PrBaCo_2O_{5+\delta}$ by low energy ion

scattering.[36-37] Fig. 3d shows that on reducing O-PBFC, smaller exsolved particles are formed in comparison to R-PBFC. This observation establishes the cyclic regeneration of the nanocatalyst with likely improved catalytic activity expected from decreased particle size.[38]

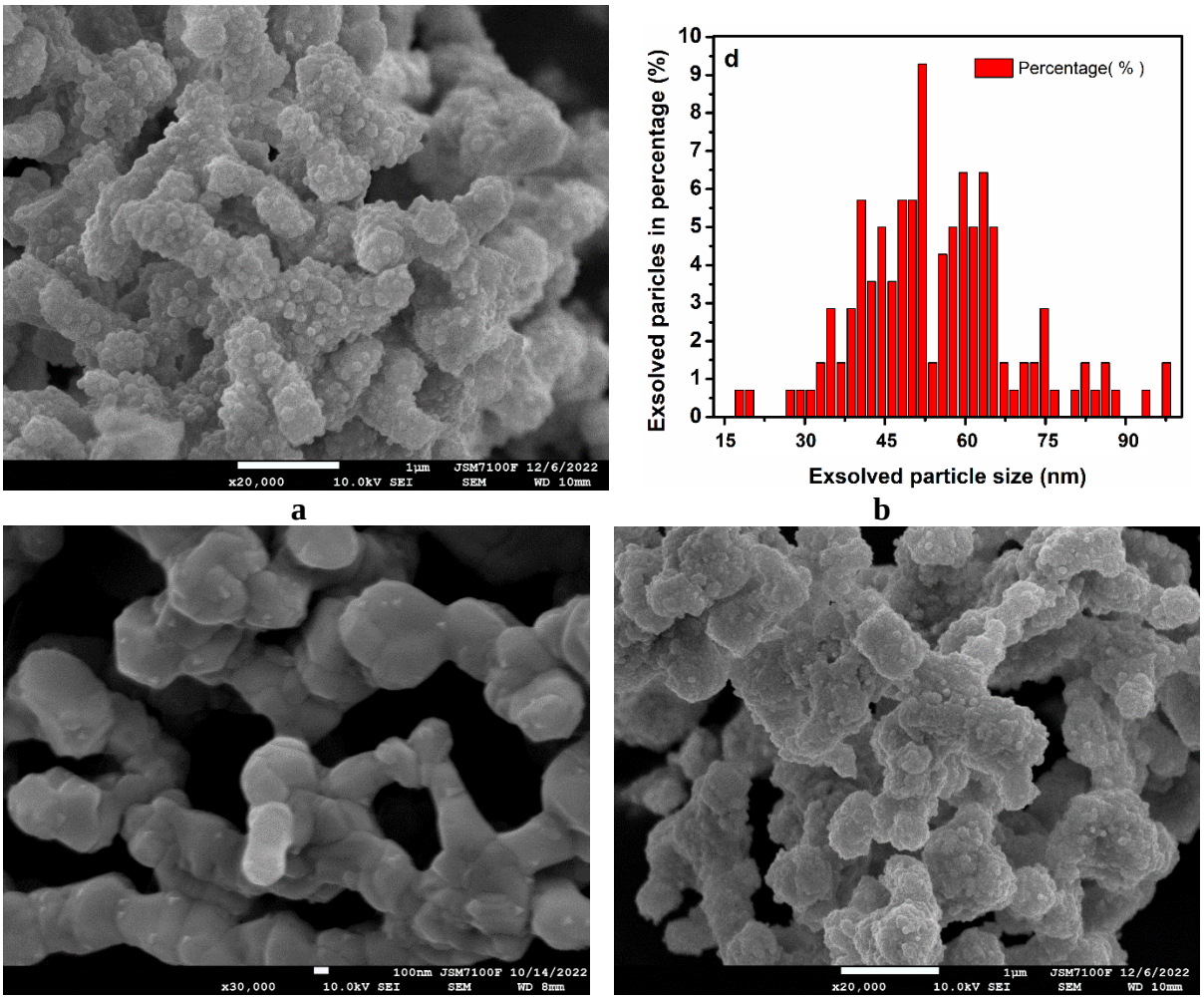

Figure 3. SEM images of PBFC after various treatments: (a) reduction and(b) size distribution of the Co-Fe alloy particles, (c) re-oxidation, (d) re-reduction.

Further information on R-PBFC is obtained from high-resolution TEM images. Fig. 4a shows a nanoparticle of ~ 50 nm diameter partially embedded in the support. From EDS analysis (Fig. 4b), the composition consists of mainly Co (90 at. %) and some Fe (10 at. %) in consistency with element mapping (Figs. 4 c-h), as expected from the lower segregation energy of Fe.[39,40]

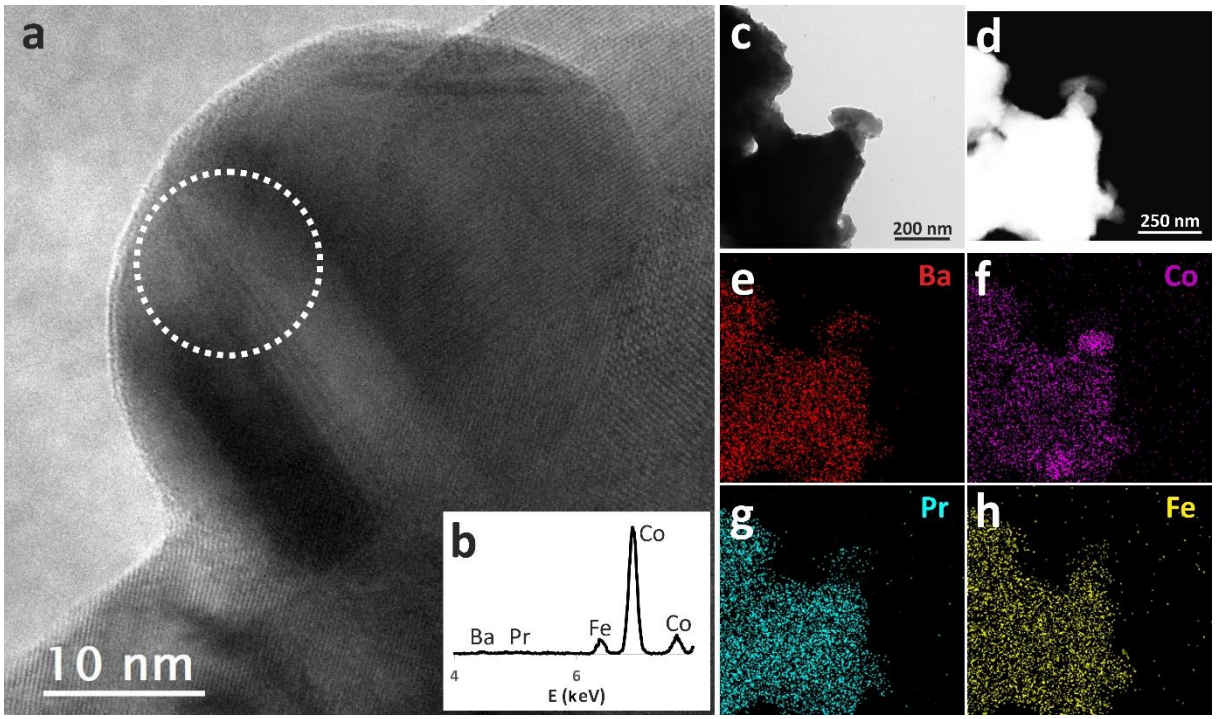

Figure 4. TEM images of R-PBFC: (a) magnified HRTEM image, and (b) EDS of an exsolved nanoparticle, (c) TEM, (d) high-angle annular dark-field image, and (e-h) EDS element mapping of the metals.

In situ neutron diffraction

i) Cycle under wet 5% H_2/He (3% H_2O)

The neutron pattern collected at T = 20 °C before heating is displayed in Fig. 5. All the peaks could be indexed in the tetragonal unit cell (S.G. *P*4/*mmm*) giving the lattice parameters, a ~ 3.90595 (5) Å and c ~ 7.73215 (4) Å. Refinement of the oxygen sites leads to the stoichiometric composition, $PrBaFeCoO_{5.92(8)}$ whose structural parameters are listed in Table 2.

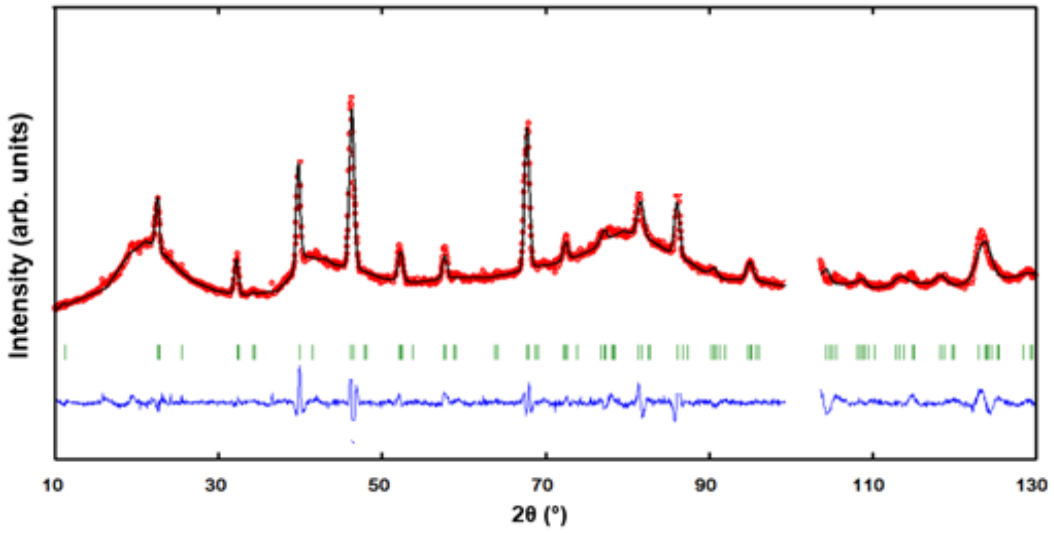

Figure 5. Rietveld plot based on neutron diffraction data collected on S-PBFC at *T* ~ 20 °C. The excluded region (99-104°, 2*θ*) contains contributions from the sample environment.

Table 2. Structural parameters of S-PrBaFeCoO$_{5+\delta}$ at 20 °C (S.G. *P*4/*mmm*, *a* = 3.90595(5) Å, *c* = 7.73215 (4) Å); R_{wp} = 2.54 %, R_p = 1.98 %, χ^2 = 1.85. *Fixed.

Atom	*x*	*y*	*z*	B_{iso}	Occupancy
Pr	0.0	0.0	0.0	1.172 (2)	1*
Ba	0.0	0.0	0.5	1.193 (2)	1*
Fe	0.5	0.5	0.25	1.176 (2)	1*
Co	0.5	0.5	0.25	1.176 (2)	1*
O1	0.5	0.5	0.0	2.070 (2)	0.98 (3)
O2	0.5	0.5	0.5	2.009 (2)	1.01 (1)
O3	0.50	0.0	0.2 2(2)	1.190 (2)	0.99 (1)

The sample was heated under wet 5% H_2 /He at a rate of 10 °C min^{-1} while data were collected at 10-minute intervals (Fig. 6a). When the temperature exceeded 200 °C, the oxygen occupancy at the O1 site within the Pr-layer decreased progressively until the O1-site emptied at 500 °C (Fig. 6b) and the composition was refined to PrBaCoFeO$_{5.00(2)}$. Meanwhile oxygen is being lost, the *a*-lattice parameter increases steeply due to increasing ionic radii of the transition metal ions $(FeCo)^{4+,3+} \rightarrow (FeCo)^{3+,2+}$.[41] Once the O1 lost is over at *T* ~ 500 °C, further heating/cooling induced linear variation of the lattice parameter due to the only thermal expansion dependence.

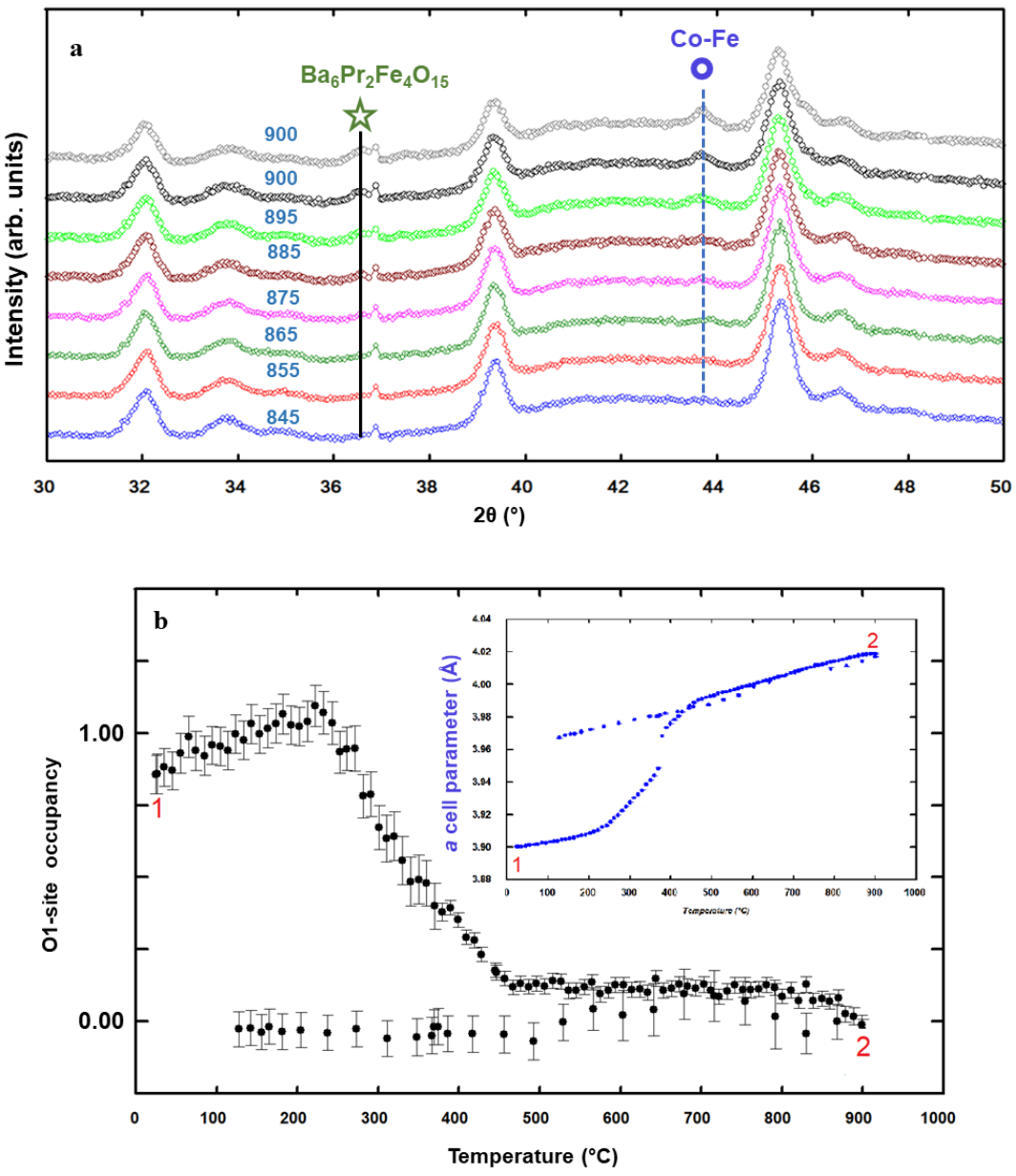

Figure 6. (a) Neutron patterns collected on heating S-PBFC under wet 5% H_2/He; the average temperature is indicated on each pattern, (b) Evolution of O1-site occupancy throughout a heating/cooling cycle, and *a*-lattice parameter in the insert with the numbers 1 and 2 referring to the start of heating and cooling, respectively.

When the temperature approached 855 °C (Fig. 6a), a peak related to a Co-Fe alloy (S.G. *Im*-3*m*) emerged at 2θ ~ 43.5° and grew on further heating. At the same time, few weak peaks related to $Ba_6Pr_2Fe_4O_{15}$ are observed in the 2θ range of 36 - 38° in consistency with the XRD of R-PBFC (Fig. 2b). Since exsolution occurs after the achievement of oxygen loss (850 °C

versus 500 °C), the stabilization of metals on the surface seems to be induced by the creation of oxygen vacancies, as reported for the layered double perovskite manganates, $PrBaMn_{1.7}M_{0.3}O_{5+\delta}$ (*M* = Ni, Co).[39] The Rietveld profile at 900 °C (Fig. 7) was fitted with a main layered perovskite phase, $PrBaCo_{0.955}Fe_{0.995}O_5$ (~ 90 wt. %) whose lattice parameters are listed in Table 3, and two minor phases Co-Fe (~ 6 wt.%) and $Ba_6Pr_2Fe_4O_{15}$ (~ 4 wt. %).

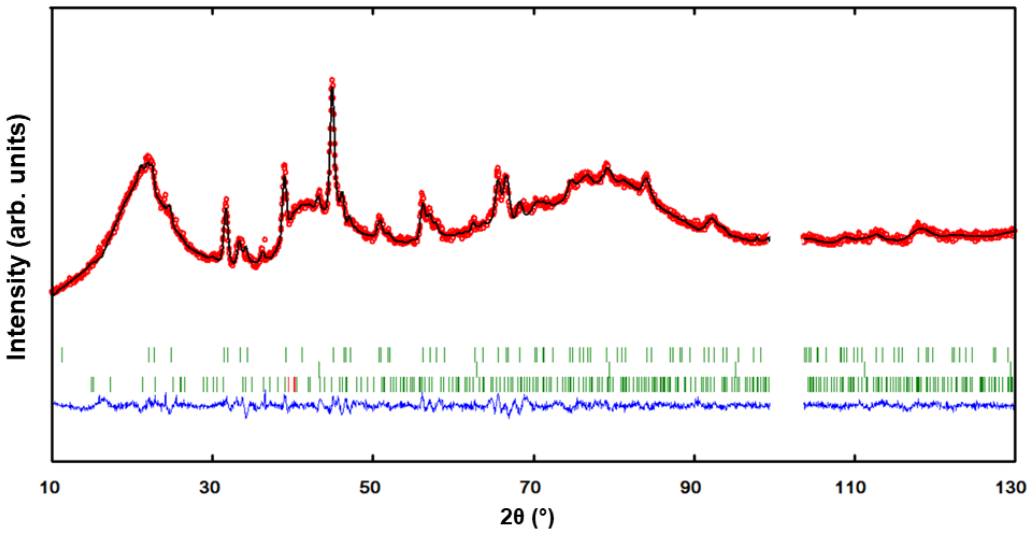

Figure 7. Rietveld plot of the neutron data collected at *T* = 900 °C under wet 5% H_2/He. First, second, and third row tick marks refer to R-PBFC, Co-Fe alloy, and $Ba_6Pr_2Fe_4O_{15}$, respectively. The excluded region contains contributions from the sample environment.

Table 3. Structural parameters of R-PBFC at 900 °C (S.G. *P4/mmm*, *a* = 4.0041 (2) Å, *c* = 7.80959 (5) Å); R_{wp} = 2.23 %, R_p = 1.65 %, χ^2 = 2.72. * Fixed, $^+$constrained to be the same.

Atom	*x*	*y*	*z*	B_{iso}	Occupancy
Pr	0.0	0.0	0.0	2.136 (2)	1*
Ba	0.0	0.0	0.5	2.159 (2)	1*
Fe	0.5	0.5	0.25	2.460 (1)	0.995 (1)
Co	0.5	0.5	0.25	2.460 (1)	0.955 (1)
O1	0.5	0.5	0.0	3.031 (2)$^+$	0.003 (3)
O2	0.5	0.5	0.5	3.031 (2)$^+$	1.002 (3)
O3	0.50	0.0	0.20 (2)	4.018 (2)	1.001 (2)

Oxidizing cycle in air

After cooling under hydrogen, the sample was heated in air at a rate of 10 °C min^{-1} up to 900 °C. While the temperature increases, the contribution from Co-Fe and $Ba_6Pr_2Fe_4O_{15}$ phases decrease progressively as noticed by the decrease of their reflections (Fig. 8). At T ~ 800 °C, those minor phases were no more detected suggesting complete reversibility of Co-Fe exsolution/dissolution in PBFC, in consistency with XRD and electron microscopy observations. In contrast to the spherical Co-Fe nanoparticles exsolved from the $Sr_2Fe_{1.35}Mo_{0.45}Co_{0.2}O_{6-\delta}$ that firstly oxidize to $CoFe_2O_4$ before dissolving into the bulk, we did not detect the presence of $(Co,Fe)_3O_4$ or transition metal oxides (FeO, Fe_2O_3, CoO, Co_3O_4) in our *in situ* neutron experiment. Therefore, if the alloy NPs oxidized before their dissolution in PBFC, such oxidation should be very fast.

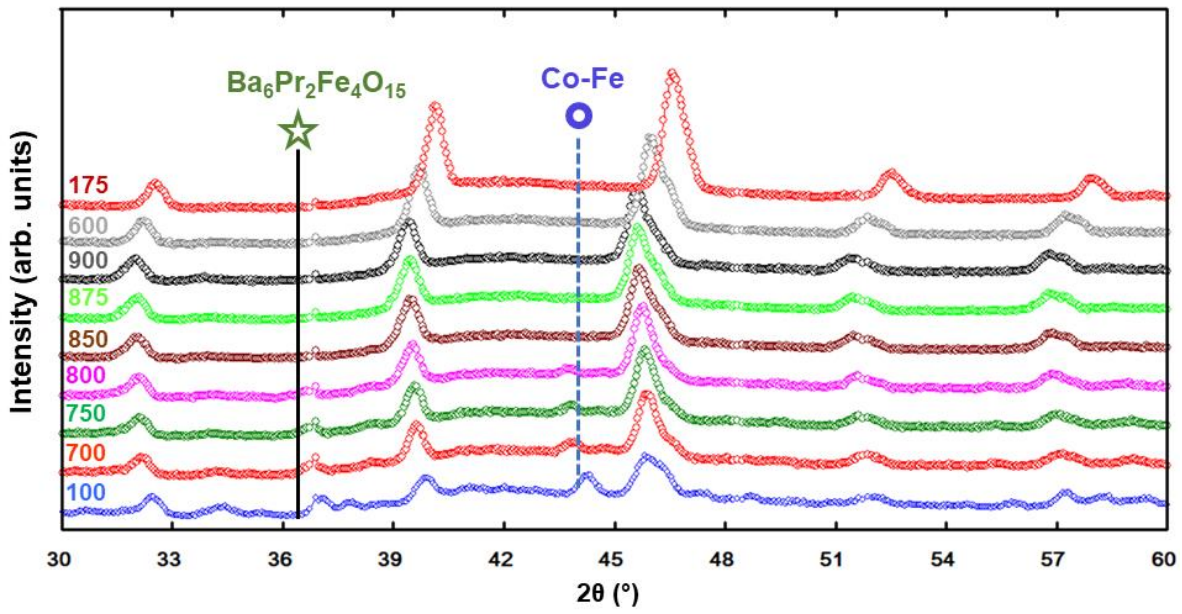

Figure 8. Neutron powder patterns collected throughout a heating/cooling cycle in air. The average temperature is indicated on each pattern. Time increases upward.

Indeed, the neutron data collected at the end of the oxidizing cycle (Fig. 9) are fitted with a single layered double perovskite $PrBaFeCoO_{5+\delta}$ whose cell parameters are close to those of the original composition (Table 4). Since the structure of the parent compound was maintained during the exsolution process, and the phase change was not too large, the dissolution of the nanoparticles in the bulk was anticipated, especially at temperatures close to the annealing

temperature. Moreover, redox exsolution reversibility is easier for *A*-site stoichiometric compositions such as $La_{0.3}Sr_{0.7}Cr_{0.3}Fe_{0.6}Co_{0.1}O_{3-\delta}$[15, 42] and Co-doped $Sr_2Fe_{1.5}Mo_{0.5}O_{6-\delta}$,[33] whereas A-site deficient compositions, as in $La_{0.7}Ce_{0.1}Co_{0.3}Ni_{0.1}Ti_{0.6}O_3$, make redissolution less favorable.[43]

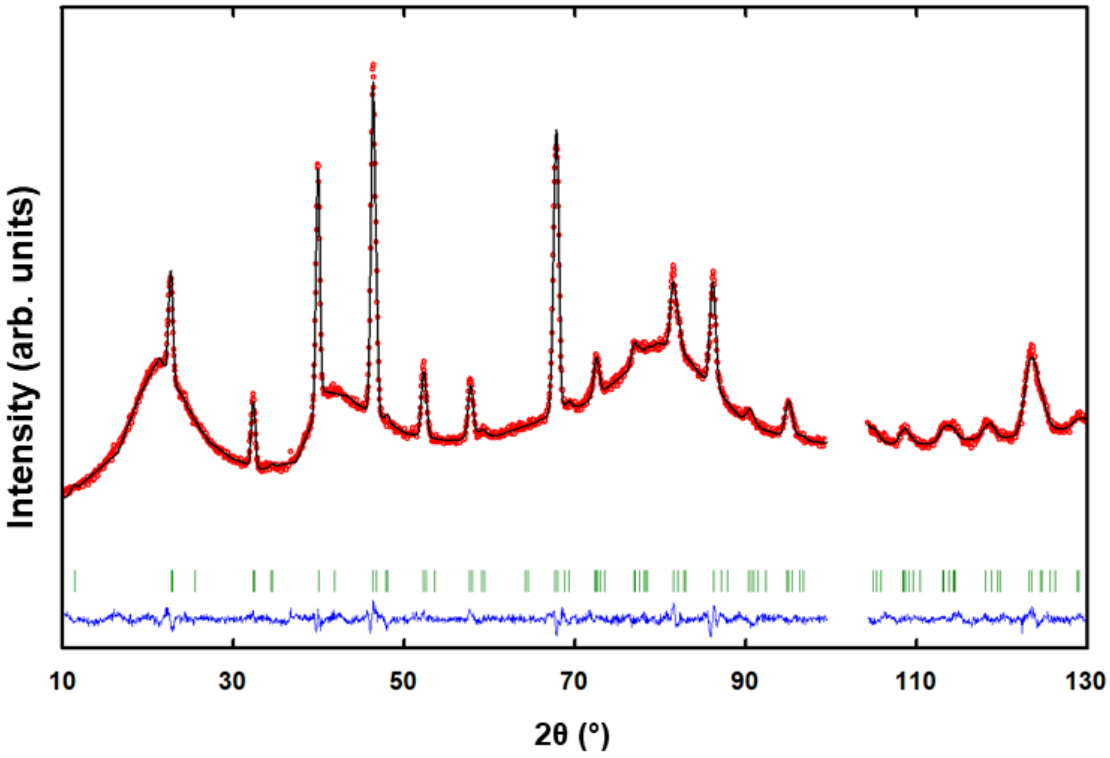

Figure 9. Rietveld plot of O-PBFC at the end of the oxidizing cycle at ~ 60 °C. The excluded region contains contributions from the sample environment.

Table 4. Structural parameters of O-PBFC (S.G. *P*4/*mmm*, *a* = 3.97348 (2) Å, *c* = 7.86199 (6) Å) at the end of the oxidizing cycle; Rwp = 2.56 %, R_p = 1.82 %, χ^2 = 3.57.

Atom	*x*	*y*	*z*	B_{iso}	Occupancy
Pr	0.0	0.0	0.5	0.9 (2)	1*
Ba	0.0	0.0	0.0	1.4(2)	1*
Fe	0.5	0.5	0.25	1.2(2)	1*
Co	0.5	0.5	0.25	1.2 (2)	1*
O1	0.5	0.5	0.0	2.5 (2)	1.01 (1)
O2	0.5	0.0	0.28 (1)	2.5 (2)	1.01 (1)
O3	0.5	0.5	0.5	2.9 (2)	0.98 (2)

Evaluation of the catalytic activity for DRM

The DRM reaction is highly endothermic (Eq. 1, $\Delta H° = 247$ kJ mol^{-1}) which usually requires temperatures above 800 °C to proceed efficiently. In addition, simultaneous side reactions like the Reverse Water Gas shift (RWGS, Eq. 2) drop the H_2/CO ratio below 1:

$$CO_2 + H_2 \rightarrow CO + H_2O \qquad \text{(Eq. 2)} \qquad \Delta H° = 41 \text{ kJ mol}^{-1}. \qquad (2)$$

The temperature-dependent tests were achieved by decreasing the temperature from 900 to 800 °C. At 900 °C, CO_2 conversion reached ~ 36.1 % and drops to ~ 19.6 % at 850 °C, and ~ 6.9% at 800 °C (Fig. 10). At the same time, CO selectivity under steady-state conditions was ~ 47.7 % at 900 °C and decreases to ~ 22.6 % at 850 °C, and ~ 8.6 % at 800 °C (Fig. 10). CO_2 conversion and CO selectivity values for R-PBFC are much better than those measured for the related $PrBaMn_{1.7}Co_{0.3}O_{5+\delta}$ and $PrBaMn_2CoO_{5+\delta}$ catalysts, and close to values assessed for Fe-infiltrated $PrBaMn_{1.7}Co_{0.3}O_{5+\delta}$ (Table 5).[27] At all temperatures, CO_2 conversion exceeds CH_4 conversion stating for the contribution of the simultaneous RWGS reaction. The H_2/CO ratio increases with temperature; from 0.075 (800 °C) to 0.152 (850 °C), and 0.3275 (900 °C) as shown in Fig. 10. Such increase is anticipated because the DRM reaction is more endothermic than the RWGS reaction.[44]

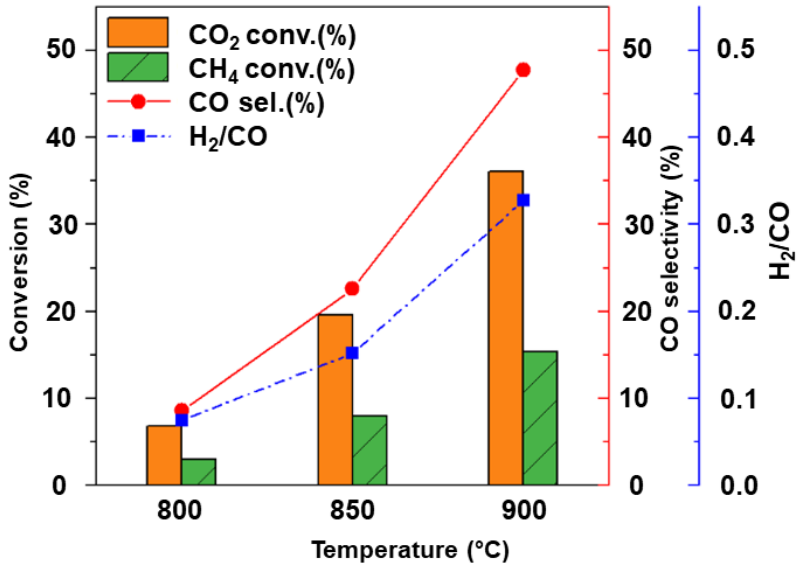

Figure 10. Catalytic performance of PBFC for DRM: CO_2 & CH_4 conversion, CO selectivity, and H_2/CO at 800, 850, and 900 °C.

Long-term tests at 800 °C (Fig. 11) showed that CO_2 and CH_4 conversions increase slowly first due to surface modifications during the dry reforming reaction then reach steady-state conditions after ~ 50 h gas exposure. At 900 °C, CO_2 and CH_4 conversions drop during the first 40 h due to metal sintering as expected when the temperature increases,[45-46] then reach a steady-state conversion rate of ~ 28 % for CO_2 and ~ 13% for CH_4.

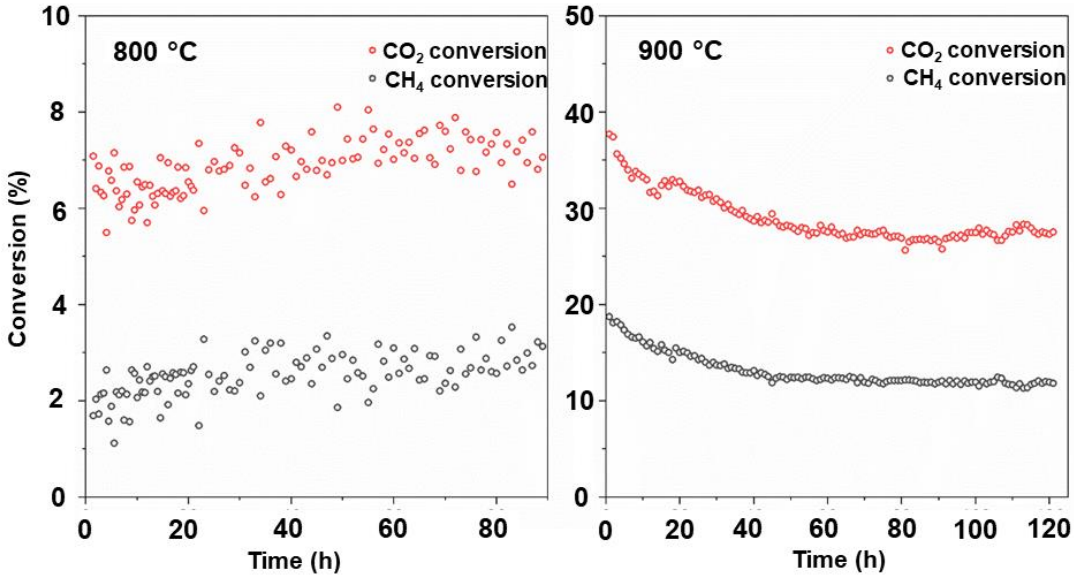

Figure 11. CO_2 and CH_4 conversions for long-term stability tests at 800 and 900 °C.

In Fe-infiltrated $PrBaMn_{1.7}Co_{0.3}O_5$,[27] long-term stability of the catalyst was explained by the oxidation of Fe to FeO_x on the surface of Co-Fe alloy and reaction of FeO_x with carbon, according to the Mars-van-Krevelen mechanism, as follows:[47]

$$Fe + xCO_2 \rightarrow FeO_x + xCO$$

$$FeO_x + xC_{Co} \rightarrow Fe + xCO + Co$$

We believe that a similar mechanism contributes in PBFC to reduce coking and ensure the stability of the catalyst in the DRM tests.

Table 5. Relevant Results on Double Perovskite catalysts for DRM.

Compound		CO_2 conversion (%) at various temperatures			
	800 °C	850 °C	900 °C	GHSV ($Lg^{-1}h^{-1}$)	Ref.
$PrBaMn_2O_{5+\delta}$	2.5,1.5, 1.5	5, 2.5, 2.5	10,12.5,7.5	30	[28]
$PrBaMn_{1.7}Ni_{0.3}O_{5+\delta}$	15	25	42.5	30	[29]
$PrBaMn_2O_{5+\delta}$	<1			96	[30]
$(PrBa)_{0.025}Mn_{1.95}O_{5+\delta}$	<1				[30]
$(PrBa)_{0.05}Mn_{1.90}O_{5+\delta}$	20				[30]
$(PrBa)_{0.1}Mn_{1.80}O_{5+\delta}$	32				[30]
$PrBaMn_{1.7}Co_{0.1}Ni._{0.2}O_{5+\delta}$	7.5	20	40	30	[28]
$PrBaMn_{1.7}Ni_{0.3}O_{5+\delta}$ (Fe-infiltrated)	15	28	45	30	[29]
$PrBaMn_{1.7}Co_{0.3}O_{5+\delta}$	2.0	4.0	12.5	30	[27]
$PrBaMn_{1.7}Co_{0.3}O_{5+\delta}$ (Fe-infiltrated)	5.0	15.0	30.0	30	[27]
$PrBaFeCoO_{5+\delta}$	6.9	19.6	36.1	30	This work

Temperature-Programmed oxidation (TPO) using thermogravimetry (TG) evaluates the thermal oxidation behavior of the spent catalyst. The TG-TPO plot (Fig. 12) shows a weight increase of ~ 3.27 % in the temperature range of 200 - 600 °C consistent with the oxidation of the R-PBC to O-PBFC and Co-Fe dissolution into the oxide host. The weight loss of ~ 2.4 % above 600 ^{o} C mainly results from the oxidation of carbon (coking) to CO_2. The amount of carbon evaluated is below 0.3 mg/(g_{cat}·h) and might originate from methane cracking[20] (CH_4 = C + 2 H) and/or CO disproportionation (2 CO = C + CO_2) during the DRM reaction.

Since neutrons provided a clear temperature point at *T* ~ 800 °C for the full reincorporation of Co-Fe in the oxide host (Fig. 8), bulk oxidation between 600 and 800 °C may overlap to small extent with carbon oxidation, but the two processes cannot be resolved by the TG method. Nevertheless, the theoretical mass needed to oxidize the Co-Fe alloy (evaluated at ~ 6 wt.% and

consisting of Co, 90 at. % and Fe, 10 at. %) is estimated at ~ 3.34%, *i.e.*, within the experimental error of the mass increase below 600 °C. Therefore, although the oxidation of the sample might compete with carbon oxidation above 600 °C, the contribution of the former process is negligible in evaluating the coking rate.

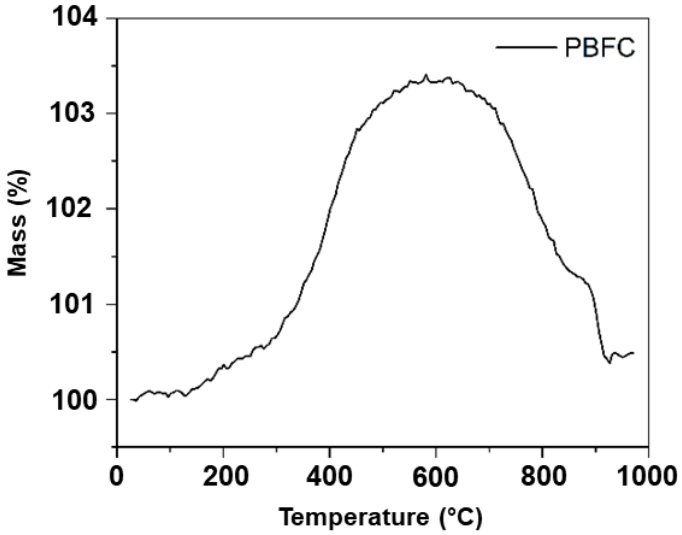

Figure 12. TG profile for the temperature-programmed oxidation (TPO) of the carbon deposits in the spent catalyst.

Finally, although the XRD pattern of the used catalyst, consisting of 80 wt.% quartz sand and 20 wt.%, gave a poor signal/noise ratio after the long-term stability tests, the main features of R-PBFC could be distinguished (Fig. S2)

Conclusion

The important point of this work is that we demonstrated that Co-Fe alloy nanoparticles that combine catalytic efficiency of Co with coking resistance of Fe, move out or into the layered double perovskite PBFC on switching between the reductive and oxidative atmospheres. Redox cycling can be used repetitively for self-regeneration of the nanocatalyst to alleviate sintering and coking issues of supported catalysts for challenging energy applications. The performance of the PBFC catalyst for the DRM reaction was stable at 800 °C for ~ 100 h duration test with negligible carbon deposition, and the CH_4 and CO_2 conversions, as well as H_2/CO selectivity were among the highest obtained for layered perovskites. To make this catalyst competitive, the size, composition, and population of the exsolved NPs might be adjusted, by altering the reduction temperature, time, and gas atmosphere.

Supporting Information

TEM image and EDS (Figure S1)

XRD (Figure S2)

Acknowledgments

This work is supported by the Ph.D. grant provided to P. Managutti by the Ministry for Higher Education, Research, and Innovation (MESRI). We thank the ILL for the beam time allowed and Alain Daramsy for his technical help at ILL. We are grateful to L. Joanny from CMEBA facility (ScanMAT, University of Rennes) for his support in SEM measurements and to S. Ollivier for her assistance in the hydrogen reduction experiments. Professor Haiqian Wang gratefully acknowledges the National Natural Science Foundation of China (Grant no.: 21872129).

References

(1) Jiang, S. P. A review of wet impregnation—An alternative method for the fabrication of high performance and nano-structured electrodes of solid oxide fuel cells. *Materials Science and Engineering: A* **2006,** *418* (1), 199-210, DOI: https://doi.org/10.1016/j.msea.2005.11.052.
(2) Ishihara, T. Nanomaterials for Advanced Electrode of Low Temperature Solid Oxide Fuel Cells (SOFCs). *J. Korean Ceram. Soc* **2016,** *53* (5), 469-477, DOI: 10.4191/kcers.2016.53.5.469.
(3) Jiang, S. P. Nanoscale and nano-structured electrodes of solid oxide fuel cells by infiltration: Advances and challenges. *International Journal of Hydrogen Energy* **2012,** *37* (1), 449-470, DOI: https://doi.org/10.1016/j.ijhydene.2011.09.067.
(4) Kim, G.; Lee, S.; Shin, J. Y.; Corre, G.; Irvine, J. T. S.; Vohs, J. M.; Gorte, R. J. Investigation of the structural and catalytic requirements for high-performance SOFC anodes formed by infiltration of LSCM. *Electrochemical and Solid-State Letters* **2009,** *12* (3), B48-B52, DOI: 10.1149/1.3065971.
(5) Liu, Z.; Liu, B.; Ding, D.; Liu, M.; Chen, F.; Xia, C. Fabrication and modification of solid oxide fuel cell anodes via wet impregnation/infiltration technique. *Journal of Power Sources* **2013,** *237*, 243-259, DOI: https://doi.org/10.1016/j.jpowsour.2013.03.025.
(6) Lou, X.; Liu, Z.; Wang, S.; Xiu, Y.; Wong, C. P.; Liu, M. Controlling the morphology and uniformity of a catalyst-infiltrated cathode for solid oxide fuel cells by tuning wetting property. *Journal of Power Sources* **2010,** *195* (2), 419-424, DOI: https://doi.org/10.1016/j.jpowsour.2009.07.048.
(7) Neagu, D.; Oh, T.-S.; Miller, D. N.; Ménard, H.; Bukhari, S. M.; Gamble, S. R.; Gorte, R. J.; Vohs, J. M.; Irvine, J. T. S. Nano-socketed nickel particles with enhanced coking resistance grown in situ by redox exsolution. *Nature Communications* **2015,** *6*, 8120, DOI: 10.1038/ncomms9120
https://www.nature.com/articles/ncomms9120#supplementary-information.
(8) Aramouni, N. A. K.; Touma, J. G.; Tarboush, B. A.; Zeaiter, J.; Ahmad, M. N. Catalyst design for dry reforming of methane: Analysis review. *Renewable and Sustainable Energy Reviews* **2018,** *82*, 2570-2585, DOI: https://doi.org/10.1016/j.rser.2017.09.076.
(9) Li, Y.; Gan, Y.; Wang, Y.; Xie, K.; Wu, Y. Composite cathode based on Ni-loaded La0.75Sr0.25Cr0.5Mn0.5O3−δ for direct steam electrolysis in an oxide-ion-conducting solid oxide electrolyzer. *International Journal of Hydrogen Energy* **2013,** *38* (25), 10196-10207, DOI: https://doi.org/10.1016/j.ijhydene.2013.06.057.
(10) Li, S.; Qin, Q.; Xie, K.; Wang, Y.; Wu, Y. High-performance fuel electrodes based on NbTi0.5M0.5O4 (M = Ni, Cu) with reversible exsolution of the nano-catalyst for steam electrolysis. *Journal of Materials Chemistry A* **2013,** *1* (31), 8984-8993, DOI: 10.1039/C3TA10404D.
(11) Tanaka, H.; Taniguchi, M.; Uenishi, M.; Kajita, N.; Tan, I.; Nishihata, Y.; Mizuki, J. i.; Narita, K.; Kimura, M.; Kaneko, K. Self-Regenerating Rh- and Pt-Based Perovskite Catalysts for Automotive-Emissions Control. *Angewandte Chemie International Edition* **2006,** *45* (36), 5998-6002, DOI: https://doi.org/10.1002/anie.200503938.
(12) Dong, G.; Yang, C.; He, F.; Jiang, Y.; Ren, C.; Gan, Y.; Lee, M.; Xue, X. Tin doped PrBaFe2O5+δ anode material for solid oxide fuel cells. *RSC Advances* **2017,** *7* (37), 22649-22661, DOI: 10.1039/C7RA03143B.
(13) Son, S. J.; Kim, D.; Park, H. J.; Joo, J. H. Investigation of oxygen ion transport and surface exchange properties of PrBaFe2O5+δ. *Journal of the European Ceramic Society* **2021,** *41* (4), 2691-2698, DOI: https://doi.org/10.1016/j.jeurceramsoc.2020.11.022.

(14) Yang, C.; Yang, Z.; Jin, C.; Xiao, G.; Chen, F.; Han, M. Sulfur-Tolerant Redox-Reversible Anode Material for Direct Hydrocarbon Solid Oxide Fuel Cells. *Advanced Materials* **2012,** *24* (11), 1439-1443, DOI: https://doi.org/10.1002/adma.201104852.
(15) Lai, K.-Y.; Manthiram, A. Self-Regenerating Co–Fe Nanoparticles on Perovskite Oxides as a Hydrocarbon Fuel Oxidation Catalyst in Solid Oxide Fuel Cells. *Chemistry of Materials* **2018,** *30* (8), 2515-2525, DOI: 10.1021/acs.chemmater.7b04569.
(16) Bhattar, S.; Abedin, M. A.; Kanitkar, S.; Spivey, J. J. A review on dry reforming of methane over perovskite derived catalysts. *Catalysis Today* **2021,** *365*, 2-23.
(17) Usman, M.; Wan Daud, W. M. A.; Abbas, H. F. Dry reforming of methane: Influence of process parameters—A review. *Renewable and Sustainable Energy Reviews* **2015,** *45*, 710-744, DOI: https://doi.org/10.1016/j.rser.2015.02.026.
(18) Zhang, G.; Liu, J.; Xu, Y.; Sun, Y. A review of CH4CO2 reforming to synthesis gas over Ni-based catalysts in recent years (2010–2017). *International Journal of Hydrogen Energy* **2018,** *43* (32), 15030-15054, DOI: https://doi.org/10.1016/j.ijhydene.2018.06.091.
(19) Jang, W.-J.; Shim, J.-O.; Kim, H.-M.; Yoo, S.-Y.; Roh, H.-S. A review on dry reforming of methane in aspect of catalytic properties. *Catalysis Today* **2019,** *324*, 15-26, DOI: https://doi.org/10.1016/j.cattod.2018.07.032.
(20) Bradford, M. C. J.; Vannice, M. A. CO2 Reforming of CH4. *Catalysis Reviews* **1999,** *41* (1), 1-42, DOI: 10.1081/CR-100101948.
(21) Sutthiumporn, K.; Maneerung, T.; Kathiraser, Y.; Kawi, S. CO2 dry-reforming of methane over La0.8Sr0.2Ni0.8M0.2O3 perovskite (M = Bi, Co, Cr, Cu, Fe): Roles of lattice oxygen on C–H activation and carbon suppression. *International Journal of Hydrogen Energy* **2012,** *37* (15), 11195-11207, DOI: https://doi.org/10.1016/j.ijhydene.2012.04.059.
(22) Xu, G.; Ma, H.; Zhong, M.; Zhou, J.; Yue, Y.; He, Z. Influence of pH on characteristics of BaFe12O19 powder prepared by sol–gel auto-combustion. *Journal of Magnetism and Magnetic Materials* **2006,** *301* (2), 383-388, DOI: https://doi.org/10.1016/j.jmmm.2005.07.014.
(23) Rodríguez-Carvajal, J. Recent advances in magnetic structure determination by neutron powder diffraction. *Physica B: Condensed Matter* **1993,** *192* (1-2), 55-69.
(24) Roisnel, T.; Rodriguez-Carvajal, J. WinPLOTR: A Windows tool for powder diffraction pattern analysis. In *Epdic 7: European Powder Diffraction, Pts 1 and 2*; Delhez, R.; Mittemeijer, E. J., Eds.; 2001; pp 118-123.
(25) Bahout, M.; Managutti, P. B.; Dorcet, V.; Le Gal La Salle, A.; Paofai, S.; Hansen, T. C. In situ exsolution of Ni particles on the PrBaMn2O5 SOFC electrode material monitored by high temperature neutron powder diffraction under hydrogen. *Journal of Materials Chemistry A* **2020,** *8* (7), 3590-3597, DOI: 10.1039/C9TA10159D.
(26) Hansen, T. C.; Henry, P. F.; Fischer, H. E.; Torregrossa, J.; Convert, P. The D20 instrument at the ILL: a versatile high-intensity two-axis neutron diffractometer. *Measurement Science and Technology* **2008,** *19* (3), 034001.
(27) Joo, S.; Kwon, O.; Kim, K.; Kim, S.; Kim, H.; Shin, J.; Jeong, H. Y.; Sengodan, S.; Han, J. W.; Kim, G. Cation-swapped homogeneous nanoparticles in perovskite oxides for high power density. *Nature Communications* **2019,** *10* (1), 697, DOI: 10.1038/s41467-019-08624-0.
(28) Kwon, O.; Kim, K.; Joo, S.; Jeong, H. Y.; Shin, J.; Han, J. W.; Sengodan, S.; Kim, G. Self-assembled alloy nanoparticles in a layered double perovskite as a fuel oxidation catalyst for solid oxide fuel cells. *Journal of Materials Chemistry A* **2018,** *6* (33), 15947-15953, DOI: 10.1039/C8TA05105D.
(29) Joo, S.; Kwon, O.; Kim, S.; Jeong, H. Y.; Kim, G. Ni-Fe Bimetallic Nanocatalysts Produced by Topotactic Exsolution in Fe deposited PrBaMn1.7Ni0.3O5+δ for Dry Reforming of Methane. *Journal of The Electrochemical Society* **2020,** *167* (6), 064518, DOI: 10.1149/1945-7111/ab8390.

(30) Managutti, P. B.; Tymen, S.; Liu, X.; Hernandez, O.; Prestipino, C.; Le Gal La Salle, A.; Paul, S.; Jalowiecki-Duhamel, L.; Dorcet, V.; Billard, A.; Briois, P.; Bahout, M. Exsolution of Ni Nanoparticles from A-Site-Deficient Layered Double Perovskites for Dry Reforming of Methane and as an Anode Material for a Solid Oxide Fuel Cell. *ACS Applied Materials & Interfaces* **2021,** *13* (30), 35719-35728, DOI: 10.1021/acsami.1c08158.
(31) Wan, T.; Zhu, A.; Guo, Y.; Wang, C.; Huang, S.; Chen, H.; Yang, G.; Wang, W.; Shao, Z. Co-generation of electricity and syngas on proton-conducting solid oxide fuel cell with a perovskite layer as a precursor of a highly efficient reforming catalyst. *Journal of Power Sources* **2017,** *348*, 9-15, DOI: https://doi.org/10.1016/j.jpowsour.2017.02.074.
(32) Jin, F.; Liu, X.; Chu, X.; Shen, Y.; Li, J. Effect of nonequivalent substitution of Pr3+/4+ with Ca2+ in PrBaCoFeO5+δ as cathodes for IT-SOFC. *Journal of Materials Science* **2021,** *56* (2), 1147-1161, DOI: 10.1007/s10853-020-05375-y.
(33) Lv, H.; Lin, L.; Zhang, X.; Song, Y.; Matsumoto, H.; Zeng, C.; Ta, N.; Liu, W.; Gao, D.; Wang, G.; Bao, X. In Situ Investigation of Reversible Exsolution/Dissolution of CoFe Alloy Nanoparticles in a Co-Doped Sr2Fe1.5Mo0.5O6−δ Cathode for CO2 Electrolysis. *Advanced Materials* **2020,** *32* (6), 1906193, DOI: https://doi.org/10.1002/adma.201906193.
(34) Lu, C.; Niu, B.; Yi, W.; Ji, Y.; Xu, B. Efficient symmetrical electrodes of PrBaFe2-xCoxO5+δ (x=0, 0.2,0.4) for solid oxide fuel cells and solid oxide electrolysis cells. *Electrochimica Acta* **2020,** *358*, 136916, DOI: https://doi.org/10.1016/j.electacta.2020.136916.
(35) Yang, C.; Li, J.; Lin, Y.; Liu, J.; Chen, F.; Liu, M. In situ fabrication of CoFe alloy nanoparticles structured (Pr0.4Sr0.6)3(Fe0.85Nb0.15)2O7 ceramic anode for direct hydrocarbon solid oxide fuel cells. *Nano Energy* **2015,** *11*, 704-710, DOI: https://doi.org/10.1016/j.nanoen.2014.12.001.
(36) Druce, J.; Téllez, H.; Burriel, M.; Sharp, M. D.; Fawcett, L. J.; Cook, S. N.; McPhail, D. S.; Ishihara, T.; Brongersma, H. H.; Kilner, J. A. Surface termination and subsurface restructuring of perovskite-based solid oxide electrode materials. *Energy & Environmental Science* **2014,** *7* (11), 3593-3599, DOI: 10.1039/C4EE01497A.
(37) Téllez, H.; Druce, J.; Ju, Y.-W.; Kilner, J.; Ishihara, T. Surface chemistry evolution in LnBaCo2O5 + δ double perovskites for oxygen electrodes. *International Journal of Hydrogen Energy* **2014,** *39* (35), 20856-20863, DOI: https://doi.org/10.1016/j.ijhydene.2014.06.102.
(38) Che, M.; Bennett, C. O. The Influence of Particle Size on the Catalytic Properties of Supported Metals. In *Advances in Catalysis*; Eley, D. D.; Pines, H.; Weisz, P. B., Eds.; Academic Press: 1989; pp 55-172.
(39) Kwon, O.; Sengodan, S.; Kim, K.; Kim, G.; Jeong, H. Y.; Shin, J.; Ju, Y.-W.; Han, J. W.; Kim, G. Exsolution trends and co-segregation aspects of self-grown catalyst nanoparticles in perovskites. *Nature Communications* **2017,** *8*, 15967, DOI: 10.1038/ncomms15967 https://www.nature.com/articles/ncomms15967#supplementary-information.
(40) Neagu, D.; Tsekouras, G.; Miller, D. N.; Ménard, H.; Irvine, J. T. S. In situ growth of nanoparticles through control of non-stoichiometry. *Nature Chemistry* **2013,** *5*, 916-923, DOI: 10.1038/nchem.1773 https://www.nature.com/articles/nchem.1773#supplementary-information.
(41) Shannon, R. D. Revised effective ionic radii and systematic studies of interatomic distances in halides and chalcogenides. *Acta Crystallographica Section A* **1976,** *32* (5), 751-767.
(42) da Silva, F. S.; de Souza, T. M. Novel materials for solid oxide fuel cell technologies: A literature review. *International Journal of Hydrogen Energy* **2017,** *42* (41), 26020-26036, DOI: https://doi.org/10.1016/j.ijhydene.2017.08.105.
(43) Neagu, D.; Papaioannou, E. I.; Ramli, W. K. W.; Miller, D. N.; Murdoch, B. J.; Ménard, H.; Umar, A.; Barlow, A. J.; Cumpson, P. J.; Irvine, J. T. S.; Metcalfe, I. S. Demonstration of chemistry at a point through restructuring and catalytic activation at anchored nanoparticles. *Nature Communications* **2017,** *8* (1), 1855, DOI: 10.1038/s41467-017-01880-y.

(44) Zhao, T.; Zhao, J.; Tao, X.; Yu, H.; Li, M.; Zeng, J.; Wang, H. Highly active and thermostable submonolayer La(NiCo)OΔ catalyst stabilized by a perovskite LaCrO3 support. *Communications Chemistry* **2022,** *5* (1), 70, DOI: 10.1038/s42004-022-00686-4.
(45) Kyriakou, V.; Neagu, D.; Zafeiropoulos, G.; Sharma, R. K.; Tang, C.; Kousi, K.; Metcalfe, I. S.; van de Sanden, M. C. M.; Tsampas, M. N. Symmetrical Exsolution of Rh Nanoparticles in Solid Oxide Cells for Efficient Syngas Production from Greenhouse Gases. *ACS Catalysis* **2020,** *10* (2), 1278-1288, DOI: 10.1021/acscatal.9b04424.
(46) Vecino-Mantilla, S.; Quintero, E.; Fonseca, C.; Gauthier, G. H.; Gauthier-Maradei, P. Catalytic Steam Reforming of Natural Gas over a New Ni Exsolved Ruddlesden-Popper Manganite in SOFC Anode Conditions. *ChemCatChem* **2020,** *12* (5), 1453-1466, DOI: https://doi.org/10.1002/cctc.201902306.
(47) Bian, Z.; Das, S.; Wai, M. H.; Hongmanorom, P.; Kawi, S. A Review on Bimetallic Nickel-Based Catalysts for CO2 Reforming of Methane. *ChemPhysChem* **2017,** *18* (22), 3117-3134, DOI: https://doi.org/10.1002/cphc.201700529.